INDIAN JOURNAL OF SCIENCE AND TECHNOLOGY

ORIGINAL ARTICLE

Influence of Thickness on Structural, Morphological, Compositional and Optical Properties of RF-Sputtered Al:ZnO Thin Films

S Uday Balegar[1], R Shashidhar[2], A Raghu[1,3]*

1 Department of Physics, Government First Grade College (Autonomous), Mandya, 571401, Karnataka, India
2 Department of Physics, J S S Academy of Technical Education, Bengaluru, 560060, Karnataka, India
3 Government Science College (Autonomous), Hassan

OPEN ACCESS

Received: 27/04/2025
Accepted: 04/05/2025
Published: 18/06/2025

Citation: Uday Balegar S, Shashidhar R, Raghu A (2025) Influence of Thickness on Structural, Morphological, Compositional and Optical Properties of RF-Sputtered Al:ZnO Thin Films. Indian Journal of Science and Technology 18(24): 1896-1907. https://doi.org/10.17485/IJST/v18i24.758

* **Corresponding author**.

raghua4@gmail.com

Funding: None

Competing Interests: None

Published By Indian Society for Education and Environment (iSee)

ISSN
Print: 0974-6846
Electronic: 0974-5645

Abstract

Objectives: The objective of this study is to investigate the manner in which the structural, morphological, compositional, and optical characteristics of aluminum-doped ZnO (AZO) thin films change with thickness. The work focuses on optical bandgap tuning through the optimization of deposition parameters and the identification of critical thickness-porosity relationships for enhanced film performance. **Method:** AZO films were deposited via RF magnetron sputtering on pre-cleaned p-type Si and quartz substrates at room temperature. Three films having thicknesses of 61 nm, 109 nm, and 160 nm were achieved by controlling deposition time and post-deposition annealing at 450°C for 1 hour in an oxygen atmosphere. Scanning electron microscopy (SEM) was used for morphological assessment, and X-ray diffraction (XRD) was used to characterize the thickness-dependent microstructural features. UV-visible spectroscopy was used to investigate the optical characteristics of the films. **Findings:** All films exhibited a hexagonal wurtzite structure and showed preferential growth along the c-axis, perpendicular to the substrate. The crystal size ranged from 9.71 to 9.90 nm, and the grain size varied between 13.69 and 19.56 nm in the films. SEM analysis revealed that film porosity decreased from 13.55% to 7.41% as the thickness increased. Stoichiometric changes in these films were observed using energy-dispersive X-ray spectroscopy (EDS). UV-Visible spectroscopy analysis revealed that both films exhibited strong transmittance (**>** 85%) in the visible region. A slight increase in the direct optical bandgap from 3.24 eV to 3.35 eV was observed. **Novelty:** This work shows how oxygen-ambient post annealing at 450°C produces RF-sputtered AZO films with great crystallinity (c-axis orientation). In order to resolve the conductivity-transparency trade-off in transparent electrodes, we uncover a crucial thickness threshold (160 nm) that strikes a balance between grain growth (19.56 nm) and optical performance (>85% transmittance, 3.24-3.35 eV bandgap). In addition to our room-temperature technique and adjustable substrate compatibility, the observed Urbach energy-thickness correlation offers

novel design guidelines for defect engineering. These results demonstrate that AZO films, which possess graded-thickness structures and a peak transparency of 92%, are excellent substitutes for ITO in solar cells and gas sensors.
Keywords: AZO thin films; thickness dependence; RF sputtering; structural; surface morphological; compositional; optical properties

1 Introduction

Due to quantum confinement impacts and large surface-to-volume ratios, metal oxide semiconductor (MOS) nanostructures exhibit unique optoelectronic properties that are distinct from bulk materials. Their solution-based fabrication, tunable morphologies, and scalable synthesis make them particularly attractive for cost-effective device applications. The applications of metal oxides span numerous and diverse fields, such as photoelectronic devices, sensors, accelerators, and high-efficiency functional devices[(1)]. Extremely versatile zinc oxide (ZnO) has several beneficial characteristics, including being an n-type transparent semiconductor oxide with a direct band-gap of 3.37 eV, a high exciton binding energy of 60 meV, outstanding chemical and thermal stability, and a hexagonal wurtzite structure. In addition to being abundant in nature, ZnO is non-toxic, affordable, and has good electrical as well as optical properties[(2)].

Doped ZnO thin films are more stable than undoped ZnO films, specifically when doped with elements from the III column of the periodic table. This kind of doping is commonly employed to stabilize carrier concentrations. For instance, doping with aluminum, a III column element, increases the optical band gap and transparency in addition to the film's low resistance as well as good stability. A prospective substitute for indium tin oxide as a transparent conducting film is aluminum-doped ZnO (AZO), making it suitable for applications in solar cells, transparent electrodes, thin-film transistors, and gas sensors[(3)]. The structural, optical, and electrical properties of AZO thin films are highly dependent on deposition techniques and post-deposition treatments. Numerous deposition techniques, such as sol-gel, chemical vapor deposition (CVD), electro-deposition, hydrothermal deposition, thermal vapor deposition, pulsed laser deposition (PLD), and radio-frequency magnetron sputtering (RF sputtering), have been previously described to produce AZO thin films[(4)]. However, the sol-gel technique suffers from weak adhesion and requires high-temperature annealing, while CVD relies on expensive precursors and difficult process management. Electrodeposition is restricted to conductive substrates and often results in non-uniform films, whereas hydrothermal deposition has a slow growth rate and scaling difficulties. Thermal vapor deposition is energy-intensive and inefficient, while PLD involves significant equipment costs and increases the difficulty in large-area deposition. On the other hand, the RF sputtering technique is preferred for the production of thin film devices, particularly where c-axis-oriented film development with strong controllability and conformity is crucial[(5)].

Despite these developments, it is still difficult to minimize post-processing complexity while maintaining good conductivity and transparency. Optimization of sputtering conditions and doping concentration (typically 2–5% Al) has been the subject of numerous studies; however, there are currently few systematic studies examining the combined effects of target geometry and oxygen annealing. The majority of AZO thin film research to date has focused on rectangular targets, ignoring the effects of other geometries, such as circular targets, on deposition uniformity and stress distribution[(6)].

A circular target, especially when used in conjunction with magnetron sputtering, creates a more uniform plasma that enhances the homogeneity and uniformity of film deposition compared to rectangular planar targets[(7)]. The use of circular targets not only reduces material waste but also improves key film properties such as conductivity, optical transparency, and grain size[(8)]. Owing to this advantage, in this study, only circular disc targets were used.

While post-deposition annealing is commonly investigated in inert (N^2/Ar) atmospheres, oxygen-rich annealing, critical for defect passivation and stoichiometric control, remains underexplored. Furthermore, there are few systematic thickness-dependent studies conducted under fixed deposition circumstances, resulting in irregular trends in structural, morphological, and optical properties.

To address these gaps, the present work employs an Al-doped ZnO circular disc target for RF sputtering to synthesize AZO films, which are then annealed at 450°C for one hour in an oxygen atmosphere.

On p-Si/quartz substrates, three films of different thicknesses were deposited under identical deposition circumstances. The results indicate that thickness affects the AZO thin films' microstructural (crystallographic orientation, size of the grain, lattice parameters, dislocation density, microstrain), morphological (grain size, porosity), compositional (stoichiometry), and optical (transmission, absorption, bandgap, Urbach energy, and dielectric constant) characteristics.

2 Methodology

2.1 Sample preparation

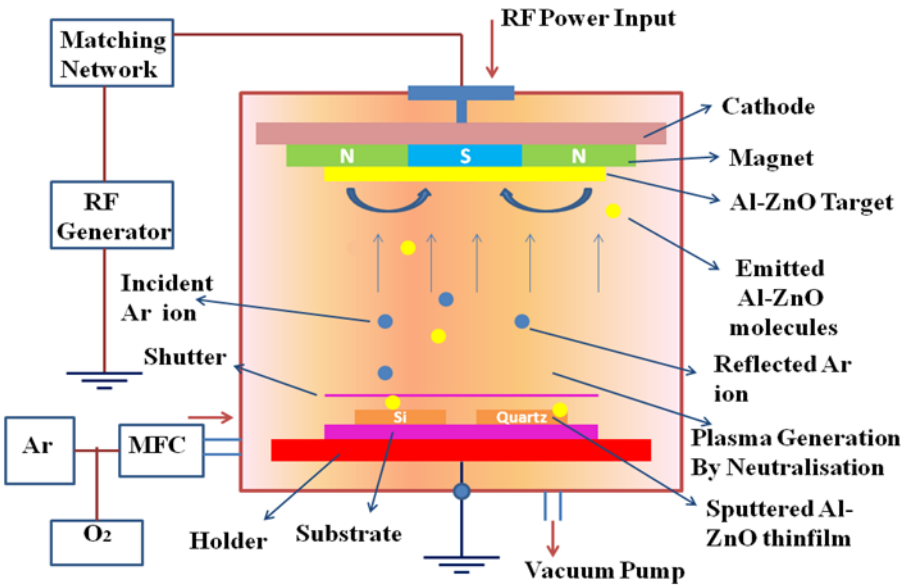

Fig 1. Schematic of the RF sputtering setup employed to deposit AZO thin films

Figure 1 shows a schematic of the RF sputtering apparatus used to deposit AZO films at room temperature. Before sputtering, a base pressure of less than 1×10^{-6} Torr was achieved by evacuating the sputtering chamber. For film deposition, argon was used as sputtering gas, with a deposition pressure of 5.31 mbar at a constant sputtering power of 140 W. The target-to-substrate distance was maintained at 10 cm. The gas flow rate and coating rates were maintained constant at 50 sccm and 0.2 nm/sec, respectively. Maintaining all the above conditions, films of varying thicknesses were deposited on pre-cleaned substrates by adjusting the sputtering time.

A commercial 3-inch diameter, 3 mm thick aluminum-doped ZnO target (Testbourne, England, 99.99% purity), backed with a 2 mm thick copper plate, served as the source material for deposition processes. On silicon and quartz substrates, distinct thin films were deposited. After deposition, the films were annealed at 450°C in an oxygen atmosphere for one hour. Each deposited film's thickness was measured using an ellipsometer (J.A. Woollam VASE) (with an accuracy of $\pm$1%). The oxygen-annealed AZO films with thicknesses of 61 nm, 109 nm, and 160 nm were designated as S1, S2, and S3, respectively.

For optical characterization, quartz substrates (area = 1 cm^2, thickness = 1 mm) were ultrasonically cleaned in sequential acetone and isopropyl alcohol baths for 5 minutes, then rinsed with deionized water and dried under a nitrogen stream. For structural and compositional analyses, p-type Si (100) wafers of identical dimensions were utilized. The wafers underwent standard RCA cleaning: organic contaminants were removed with $NH_4OH : H_2O_2 : DI$ water (1:1:5 v/v) at 78 $\pm$ 2°C for 12 minutes, followed by metallic impurity elimination using $HCl : H_2O_2 : DI$ water (1:1:6 v/v) at 78 $\pm$ 2°C for 10 minutes, with deionized water rinsing after each step.

The quartz substrates' optical transparency enabled reliable UV-Vis measurements, while silicon wafers provided optimal surfaces for XRD and SEM characterization. The rigorous RCA cleaning protocol ensured contaminant-free surfaces, which is critical for reproducible thin-film growth. Both substrates were dried under a nitrogen gas flow to prevent any surface oxidation prior to deposition.

2.2 Characterization Methods

An X-ray diffractometer (X'Pert PRO, PANalytical), equipped with monochromatic $Cuk\alpha$ radiation ($\lambda = 1.5404$Å), in the 2θ range of 20° to 80° (in 0.01° increments), and a scan rate of 1°/min was employed to examine the films' structural characteristics.

The material's morphology was analysed using a scanning electron microscope (FEI Nova NanoSEM 200) fitted with a 30 kV accelerating voltage source and energy-dispersive X-ray spectroscopy (EDS) was employed for elemental composition analysis. For optical investigation, a UV-3600 MPC 3100 UV-Vis-NIR Spectrometer was employed. The next section contains a report of the results of each measurement.

3 Results and Discussion

3.1 Structural studies - XRD analysis

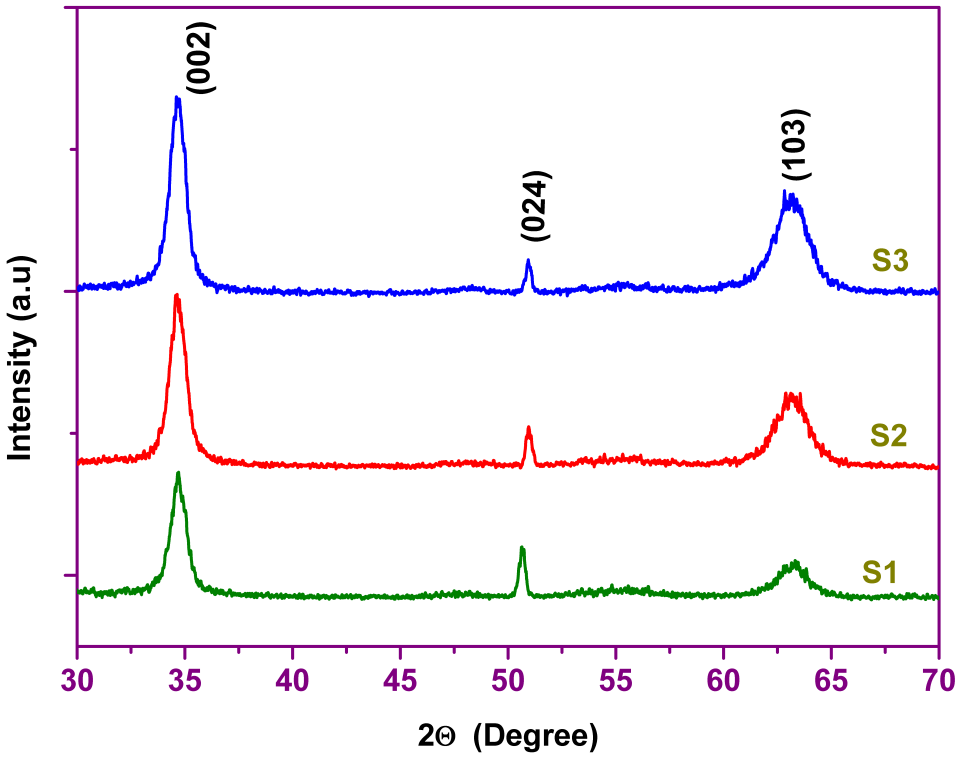

Fig 2. XRD plot of RF-sputtered Al:ZnO films

The crystalline quality of RF-sputtered AZO films was investigated through XRD analysis as a function of thickness. Figure 2 displays the XRD spectra of the AZO films. The primary peaks were found at 2θ = 34.70°, 51°, and 62.8°, corresponding to the diffraction planes (002), (024), and (103), confirming the hexagonal wurtzite structure (JCPDS #36-1451). The (024) peak at 2θ = 51° also indicates the presence of rhombohedral Al particles (JCPDS #10-0173). The observed peak shifts suggest successful doping, with Al^{3+} ions occupying Zn^{2+} lattice sites. The (002) peak intensity is stronger than that of other peaks in AZO films, indicating preferential growth along the c-axis, perpendicular to the surface of the substrate. However, all diffraction peak intensities increased with increasing film thickness with slight deviation [9].

Figure 3 shows a slight deviation of 2θ = 0.03°- 0.04° in the (002) peak position as a function of AZO film thickness. Similar deviations are also observed in the (024) and (103) peaks. These shifts in XRD peaks with film thickness are primarily due to changes in internal strain, crystallinity, and grain size within the AZO films. As the thickness increases, the (103) peak intensity becomes more prominent, indicating more textured film growth. With increasing film thickness, these factors can alter the lattice parameters, leading to the observed peak shifts [10].

After estimating the peak's Bragg diffraction angle (θ) and the full width at half maximum (FWHM, β) from the XRD data, the average crystallite size $D_{(hkl)}$ was determined using the Debye-Scherrer formula [11],

$$D_{(hkl)} = \frac{k\lambda}{\beta \cos\theta} \quad (1)$$

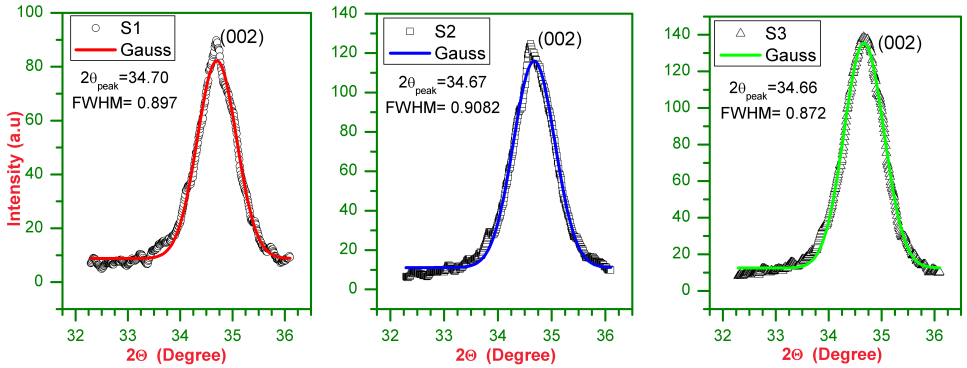

Fig 3. Gaussian fitting of the prominent (002) peak for three samples, illustrating the peak shift as a function of AZO film thickness

where $k = 0.94$ is the shape factor, and λ is the wavelength of the X-ray. Smaller $D_{(hkl)}$ values indicate finer crystallites and larger grain boundaries, which may enhance gas sensing surface area. Conversely, larger crystallites can improve electron mobility in solar cell applications. All other microscopic crystal features were calculated using these parameters [(12)-(13)].

The lattice strain (ε) quantifies lattice distortions due to defects, doping, or stress, and it is computed as:

$$\varepsilon = \frac{\beta \cos\theta}{4} \tag{2}$$

Interplanar distance (d) is calculated using Bragg's law:

$$d = \frac{\lambda}{2\sin\theta} \tag{3}$$

The changes in d indicate strain or compositional variations.

The distortion parameter (g) explains the local bending or warping of atomic planes, and is given by:

$$g = \frac{\beta}{\tan\theta} \tag{4}$$

The number of crystal defects per unit area is the dislocation density (δ), and is defined as:

$$\delta = \frac{1}{D^2} \tag{5}$$

Table 1. Structural properties of RF-sputtered AZO films as a function of thickness estimated for the intense (002) peak

Sample	βin degrees	D (nm)	$\epsilon(\times 10^{-4})$	$(\delta)(\times 10^{15}\mathrm{m}^{-2})$	(d)Å	$(g)(\times 10^{-2})$	$CI(\%)$	Grain size (nm)	(Φ)**(%)**
S1	0.897	9.71	37.3	10.61	2.583	5.011	83.55	13.69	13.55
S2	0.908	9.59	37.8	10.88	2.586	5.079	88.47	14.91	10.32
S3	0.872	9.99	36.3	10.03	2.586	4.878	95.31	19.56	7.41

Calculating the integrated intensity areas of crystalline peaks " $I_{crystal}$" and the total intensity area (crystalline + amorphous background) "I_{total}" in the XRD spectra, the crystallinity index $(CI(\%))$ is estimated as:

$$CI(\%) = \frac{I_{crystal}}{I_{total}} \times 100 \tag{6}$$

CI(%) evaluates the phase purity of the material; a higher *CI(%)* indicates a more ordered crystalline structure, which is critical for enhanced optoelectronic performance. All these crystalline properties are determined and tabulated in Table 1.

From Table 1, it is observed that as the film thickness increases, the crystallite size grows from 9.71 nm to 9.99 nm. As more crystal surfaces scatter the X-rays, the diffraction peaks become more intense. The distortion parameter decreases with

film thickness. This trend is observed because a thicker film allows for better structural development and greater crystalline perfection, leading to less distortion[14]. This is supported by the rise in the crystallinity index with thickness. With higher thickness, the material has more time for atomic diffusion and opportunity to achieve a more ordered, crystalline structure[15].

The variation in micro-crystalline properties is further analyzed by plotting dislocation density and lattice strain as a function of crystallite size (Figure 4(a)), crystallite and grain sizes as a function of AZO film thickness (Figure 4(b)). As the crystallite size increases, the probability of encountering lattice imperfections and internal stress decreases. During thin film deposition, smaller crystallites typically exhibit a higher density of defects or grain boundaries, leading to increased dislocation density and strain. Aluminum doping influences crystallite size and strain by modifying crystal growth kinetics and defect density. As shown in Figure 4(b), both crystallite and grain sizes exhibit a direct correlation with AZO film thickness. This relationship evolved from enhanced atomic mobility and extended growth time during deposition, enabling individual grains to develop larger dimensions in thicker films. The expansion of crystalline domains reduces lattice imperfections, leading to sharper diffraction peaks and a more ordered structure[16].

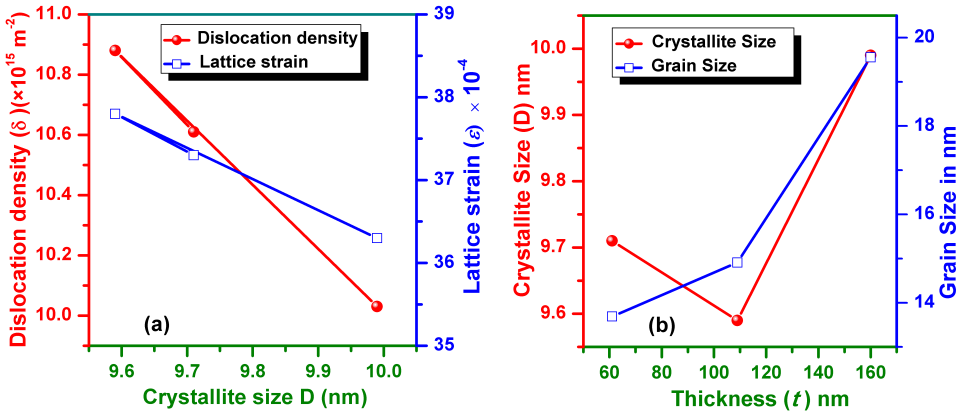

Fig 4. (a) Variation of dislocation density and lattice strain as a function of crystallite size, (b) Variation of crystallite size and grain size with AZO film thickness

Oxygen annealing of AZO thin films at 450°C reduces lattice strain by facilitating crystallite rearrangement and dislocation annihilation, while simultaneously homogenizing film density to minimize interfacial scattering and gradient effects[17].

3.2 Morphological and Compositional Studies

The SEM images with the inset histogram and EDS spectra of AZO films are shown in Figure 5. Grain sizes were measured from SEM images using ImageJ software. ImageJ measurements, while valuable, inherently have uncertainties up to +1% due to various factors, including calibration, pixel size, and edge detection. The images reveal that the grain size increases from 13.69 nm to 19.56 nm (see Table 1). The histogram-derived grain size increases with film thickness (see section 3.1 and Figure 4(b) for comparison with crystallite size). The films exhibit dense, compact, and uniform microstructures. This indicates a polycrystalline nature where individual grains are interconnected by grain boundaries[18]. The existence of grain boundaries indicates that the individual grains are connected by relatively large areas of material with different crystalline orientations. Grains are evenly spaced without significant agglomeration or clustering. This uniformity is crucial for consistent performance across the film's surface[19].

Film porosity was calculated from SEM images using ImageJ software. Porosity values (Table 1) decline from 13.55% to 7.41% with increasing film thickness. As the AZO film becomes thicker, the individual grains within the film tend to grow larger and more densely packed. This enhanced packing density reduces both pore density and average pore size[20].

The EDS study displays the peaks of zinc (Zn), oxygen (O), and aluminum (Al) elements in the AZO films, as shown in Figure 5. A prominent peak in the spectra corresponds to the silicon substrate (SiO_2). The absence of any impurity peaks in each EDS spectrum confirms the material purity of the film. Table 2 shows that both the Al atomic percentage and the O to Zn atomic ratio decline with increasing film thickness. This implies that the concentration of aluminum in the film as a whole and the amount of oxygen relative to zinc decrease with increasing AZO film thickness. The decreasing O:Zn atomic ratio with increasing film thickness indicates reduced oxygen incorporation per zinc atom, a trend potentially influenced by deposition temperature, sputtering parameters, Al-ZnO lattice interactions, and thickness-dependent dopant incorporation efficiency[21].

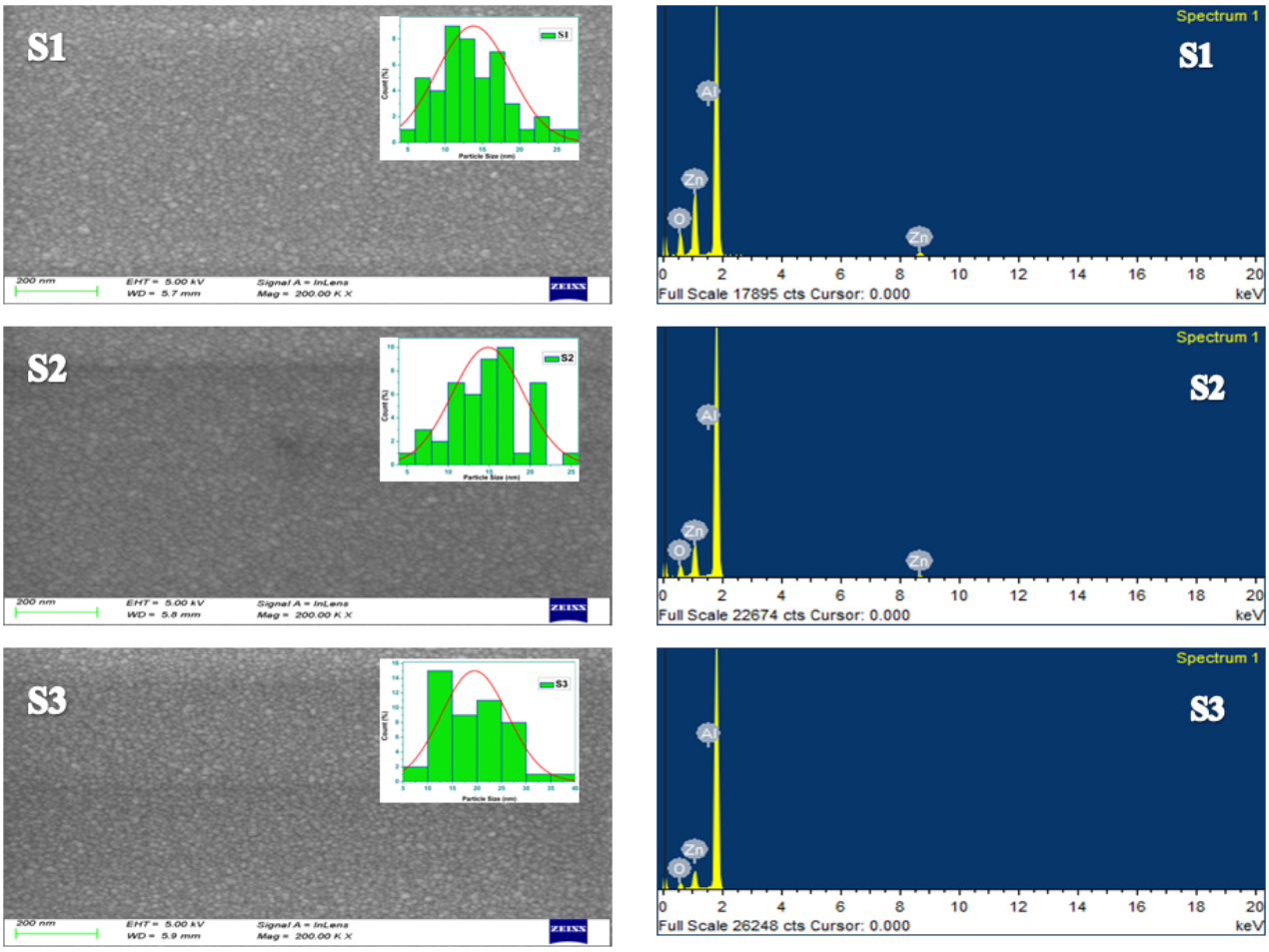

Fig 5. SEM images with inset histogram and EDS spectra of RF-sputtered AZO films as a function of thickness.

Note that, although EDS can detect the presence of oxygen, it is difficult to quantify accurately due to low X-ray fluorescence yield, self-absorption, and detector efficiency. This error in O estimation was not carried out in this study.

Table 2. Stoichiometry for all Al:ZnO thin films

Sample	Zn at (%)	O at (%)	O: Zn	Al at (%)
S1	63.93	32.31	0.50	3.76
S2	67.14	29.37	0.44	3.49
S3	68.72	28.03	0.41	3.25

3.3 Optical Characterization and Analysis

3.3.1. UV-Visible Spectra

Optical studies of AZO films typically focus on their transparent conductive properties, particularly in the visible and near-IR regions. These studies analyze parameters such as transmittance, band gap, refractive index, and extinction coefficient to understand the film's suitability for various applications like optoelectronics, solar cells, and transparent electrodes[22]. AZO films are found to exhibit high transmittance in the visible and IR region, with values often exceeding 70%. However, the transmittance in the UV region is lower.

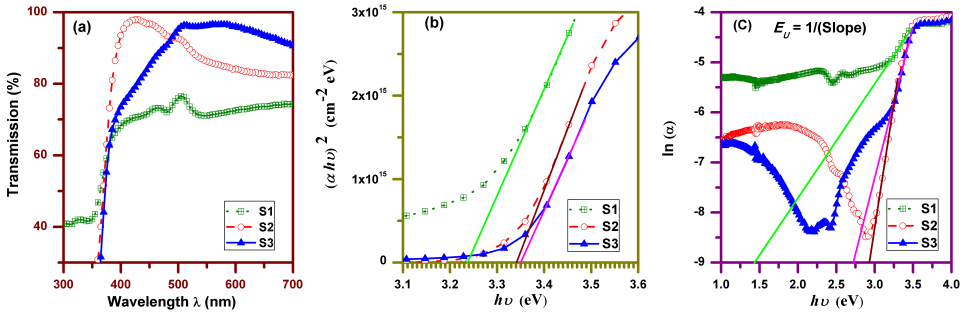

Fig 6. (a) Transmittance, (b) optical bandgap ($\mathbf{E_g}$), and (c) Urbach energy ($\mathbf{E_u}$) spectra of AZO films

The transmittance, optical bandgap, and Urbach energy spectra of the three films are displayed in Figure 6. The transmittance spectra depict an increase in transmission with film thickness. As the thickness increases from 61 nm to 160 nm, the films develop larger, more ordered crystallites, reducing defect density and porosity. This phenomenon is often observed in various thin film materials and is a key consideration in designing optical devices[23]. AZO films are used as transparent electrodes in displays, touchscreens, and other optoelectronic devices due to their high transmittance and conductivity[24].

3.3.2. Spectroscopic Measurements and Fundamental Parameters

The optical properties, such as packing density and porosity, were calculated using equations (7) and (8), respectively[25].

$$\text{Packing density, (P)}\% = \frac{(n^2{}_f - 1)(n^2{}_b + 2)}{(n^2{}_f + 2)(n^2{}_b - 1)} \times 100 \tag{7}$$

$$\text{Porosity, } (\Phi)\% = \left[1 - \frac{(n^2{}_f - 1)(n^2{}_b + 2)}{(n^2{}_f + 2)(n^2{}_b - 1)}\right] \times 100 \tag{8}$$

The symbols n_f and n_b stand for the film's and the bulk material's refractive indices. AZO has a bulk refractive index (n_b) of 1.95 and the thin film refractive indices used are 1.75, 1.8, 1.85 for AZO1, AZO2, AZO3, respectively.[26]

Absorption coefficient (α), Extinction coefficient (k), Dielectric susceptibility (χ), Optical conductivity (σ), Dielectric constant (ε_r), Optical energy band gap (E_g), and Urbach energy (E_u) were determined by studying the transmittance spectrum[27]-[28].

Let 'A' and 't' represent the optical radiation absorbance and the film thickness, respectively. The film's absorption coefficient (α) can then be calculated as

$$\alpha = \frac{2.303\ A}{t} \tag{9}$$

Using the absorption coefficient (α) of the film, the extinction coefficient (k) and other optical parameters can be calculated as follows:

$$\text{Extinction coefficient, } k = \frac{\alpha\lambda}{4\pi} \tag{10}$$

$$\text{Optical susceptibility, } \chi = \frac{n^2 - k^2 - 1}{4\pi} \tag{11}$$

$$\text{Optical conductivity, } \sigma = \frac{\alpha nc}{4\pi} \tag{12}$$

$$\text{The dielectric function's real component, } \varepsilon_r = 1 + 4\pi\chi \tag{13}$$

$$\text{The dielectric function's imaginary component, } \varepsilon_i = 2nk \tag{14}$$

where c and n denote the light's speed and the refractive index of the film.

3.3.3. *Optical energy band gap (E_g) and Urbach energy (E_u)*

The absorption coefficient (α) is utilized to ascertain the film optical band gap (E_g) which is provided by Tauc's equation as

$$(\alpha h\nu)^{\frac{1}{m}} = C\left(h\nu - E_g\right) \tag{15}$$

where C and $h\nu$ stands for the proportionality constant and the photon's energy, correspondingly. The value of the exponent ' m ' is determined by the nature of the electrical transition, and $m = \frac{1}{2}$ for a direct allowed transition. This value is utilized to calculate the optical band gap (E_g) by projecting a linear fit (Figure 6b) to the absorption coefficient's leading edge to the background level.

The Urbach energy, E_u quantifies the width of localized states near the band edge and was determined by analysing the sub-bandgap absorption region of the AZO thin films. The exponential tail of the absorption coefficient (α) follows the relation:

$$\alpha = \alpha_0 e^{\frac{h\nu}{E_u}} \Rightarrow \ln\alpha = \ln\alpha_0 + \frac{h\nu}{E_u} \tag{16}$$

where $h\nu$ is the photon energy, α_0 is the pre-exponential factor, related to the absorption. Fitting the linear region below the bandgap in a plot of $\ln\alpha$ and $h\nu$ gives slope, and the inverse of the slope yields E_u (Figure 6c). Lower E_u values indicate reduced structural disorder for thicker films (e.g., 160 nm), where improved crystallinity and oxygen annealing passivate defects like oxygen vacancies and zinc interstitials. In contrast, thinner films (61 nm) exhibit higher E_u due to greater grain boundary scattering and incomplete crystallization. This method directly correlates optical absorption with atomic-scale disorder, providing insight into defect-mediated optical losses in AZO films. All these optical parameters were estimated with the corresponding relations and shown in Table 3.

Table 3. Estimated optical parameters for RF-sputtered thin films of various thicknesses at a wavelength of $\lambda = 600$ nm

Sample	$\alpha\times10^6\text{m}^{-1}$	Φ**(%)**	P	k	χ	$\sigma\times10^{14}$	ε_r	ϵ_i
S1	5.40	15.76	84.24	0.26	0.2177	2.51	3.74	1.01
S2	1.64	11.23	88.77	0.08	0.2225	0.761	3.79	0.29
S3	0.22	8.45	91.55	0.01	0.223	0.103	3.80	0.042

3.3.4. *Thickness-Dependent Trends*

From Table 3, it can be observed that the values of packing density, optical susceptibility, real dielectric constant, and direct optical band gap increase with AZO film thickness. Thicker films exhibit enhanced atomic packing due to extended grain growth and strain relaxation, as confirmed by narrow XRD peak widths. The rise in χ and ε_r reflects the stronger electronic polarization from well-ordered Al-O-Zn bonds and reduced porosity. The real component of the dielectric constant can surge with thickness, particularly in films with a higher density of states [29].

The absorption coefficient, porosity, optical conductivity, imaginary component of the dielectric constant, and the Urbach energy tend to decrease with thickness in RF-sputtered AZO films. This is because denser and more compact films formed at higher thicknesses lead to reduced light scattering and absorption. The absorption coefficient is linked to the existence of defects, grain boundaries, and other imperfections. These flaws tend to diminish as film thickness increases. As the film thickens, porosity decreases, leading to denser and more compact layers, and the imaginary component typically decreases due to reduced absorption and scattering.

Using **equation (10)**, the extinction coefficient (k) was estimated for all wavelengths. The variation of the k values with wavelength for different film thicknesses are shown in Figure 7b. Notably, the extinction coefficient decreases as the film thickness increases in the visible range. This tunability of the k value with thickness enables tailored applications - from UV-selective absorbers (high-k value, thin films) to high-transparency electrodes. The ability to regulate the k value through

thickness control enables customized applications, emphasizing the crucial role of defect engineering in optimizing transparent conductive oxides [30].

For further analyses, estimated values of optical bandgap and Urbach energy as a function of AZO film thickness are plotted in Figure 7a. Urbach energy exhibits non-monotonic behavior, whereas optical bandgap energy exhibits a monotonic behavior with increasing film thickness. With the AZO film thickness, crystallinity increases initially due to an increase in the energy band gap. With further film thickening, the energy band gap does not increase significantly due to factors such as stress induced by the film's growth and grain boundary effects, which introduce localized states inside the band gap. Initially, when the film is 61 nm thick, the Urbach energy is high, as the material is more disordered due to the structural imperfections caused by particle bombardment during the sputtering process. However, for thicknesses of 109 nm and 160 nm, the Urbach energy decreases as the film's crystallinity improves and the material becomes more ordered [31].

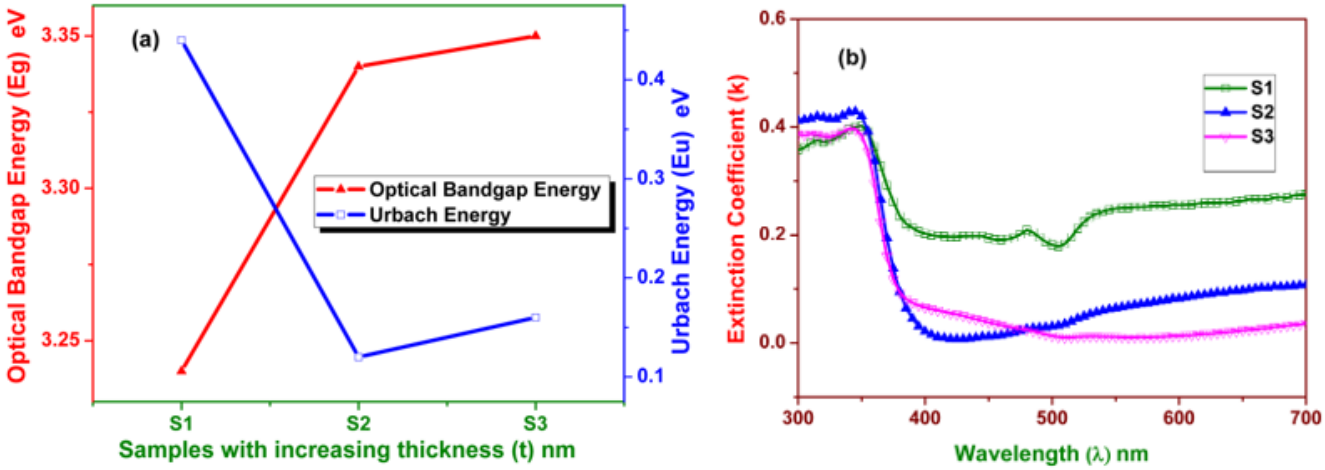

Fig 7. (a) Variation of optical bandgap ($\mathbf{E_g}$) and Urbach energy ($\mathbf{E_u}$), (b) extinction coefficient (k) vs. wavelength for three samples S1, S2 and S3.

The band gap of AZO films around 3.23 eV indicates their ability to absorb light in the UV range. The tunable optical bandgap and effective defect passivation in AZO films make them promising candidates for transparent electrodes in optoelectronic devices such as solar cells and LEDs, where precise control over thickness-dependent properties is essential. The non-monotonic behaviour of the Urbach energy serves as a valuable diagnostic tool for optimizing thin-film deposition processes, enabling the reduction of structural disorder and improvement of material quality. Furthermore, oxygen annealing at 450°C demonstrates a scalable approach to defect suppression, enhancing AZO film performance for advanced applications in flexible electronics and high-power devices by systematically reducing oxygen vacancies and sub-bandgap absorption.

Table 4. Summary table

S	D(nm)	$CI(\%)$	Grain size (nm)	$\Phi(sem)$%	Al at (%)	$\alpha\times10^6\mathrm{m}^{-1}$	E_g(eV)	E_u(eV)	Φ(opt) (%)	P	ε_r
S1	9.71	83.55	13.69	13.55	3.76	5.40	3.24	0.44	15.76	84.24	3.74
S2	9.59	88.47	14.91	10.32	3.49	1.64	3.34	0.12	11.23	88.77	3.79
S3	9.99	95.31	19.56	7.41	3.25	0.22	3.35	0.16	8.45	91.55	3.80

It is observed that with the increment of film thickness, the crystal size, crystallinity index, grain size, band gap, packing density and dielectric constant are found to increase, whereas the film porosity, absorption coefficient and Urbach energy decrease. An earlier study indicates that the most suitable thickness range for the sputtered AZO film is between 150–250 nm, which can be used as a solar cell electrode [32]. A similar kind of band gap variation is observed for 3% Al-doped AZO films [33].

The summary table depicts the influence of film thickness, aluminium doping, and oxygen annealing on the properties of RF sputtered AZO films.

4 Conclusions

High-quality AZO films with thicknesses of 61 nm, 109 nm, and 160 nm were successfully deposited via the RF magnetron sputtering technique. The films were annealed at 450°C for 1 hour in an oxygen atmosphere. The relationship between the AZO film thickness and its structural, morphological, compositional, and optical characteristics have been thoroughly studied. All of the AZO films contain hexagonal wurtzite structures with a high c-axis preferred orientation, according to structural analysis. Crystallite size increased from 9.71 nm to 9.90 nm, and the grain size grew from 13.69 nm to 19.56 nm with the increase in film thickness. SEM analysis revealed that film porosity decreased from 13.55% to 7.41% as the thickness increased. The SEM images also show that the synthesized films were dense, compact, uniform, and of good quality. Oxygen annealing at 450°C optimizes stoichiometry, reducing oxygen vacancies while maintaining Zn-rich conditions for conductivity. The inverse correlation between thickness and Urbach energy highlights the importance of defect engineering in these transparent conductive oxides. The optical transmittance spectra reveal that all synthesized AZO films exhibit high transparency (>85%) across the visible spectrum, which is a critical requirement for solar cell applications. This combination of high transparency and thickness-tunable optoelectronic properties, evidenced by Urbach energy reduction, positions the films as promising candidates for next-generation photovoltaic devices and chemical sensing platforms.

RF sputtering of AZO films, while a valuable technique for depositing thin films, faces limitations in achieving optimal optical properties, particularly at low deposition temperatures and with thin film thicknesses. These limitations include poor conductivity due to insufficient diffusion and low ionization, higher resistivity for thinner films, and compressive stress as a result of ion bombardment. These limitations can be overcome by optimizing the deposition process, using vacuum or air annealing, and exploring new material combinations. By strategically addressing these aspects, it is possible to improve the performance of RF-sputtered AZO films for various applications, including transparent conductive electrodes in solar cells and flexible display technologies.

References

1) Tan T, Hang Z, Li X, Wang S, Homewood K, Xia X, et al. Ultra-high-response heat free H2 sensor based on a WO3/Pt-ZnO thin film. *Journal of Alloys and Compounds*. 2024;979:173527. https://doi.org/10.1016/j.jallcom.2024.173527.
2) Rasmidi R, Duinong M, Chee FP. Radiation damage effects on zinc oxide (ZnO) based semiconductor devices–a review. *Radiation Physics and Chemistry*. 2021;184:109455. https://doi.org/10.1016/j.radphyschem.2021.109455.
3) Wang J, Meng C, Liu H, Hu Y, Zhao L, Wang W, et al. Application of indium tin oxide/aluminum-doped zinc oxide transparent conductive oxide stack films in silicon heterojunction solar cells. *ACS Applied Energy Materials*. 2021;4(12):13586–13592. https://doi.org/10.1021/acsaem.1c02209.
4) Raha S, Ahmaruzzaman M. ZnO nanostructured materials and their potential applications: progress, challenges and perspectives. *Nanoscale Advances*. 2022;4(8):1868–1925. https://doi.org/10.1039/D1NA00880C.
5) Liu Z, Guo Y, Li S, Chen Y, Deng K, Liu H, et al. Effects of sputtering process and annealing on the microstructure, crystallization orientation and piezoelectric properties of ZnO films. *Next Materials*. 2025;6:100429. https://doi.org/10.1016/j.nxmate.2024.100429.
6) Bussell BC, Gibson PN, Lawton J, Couture P, Sharpe MK, England J, et al. The effect of RF plasma power on remote plasma sputtered AZO thin films. *Surface and Coatings Technology*. 2022;442:128402. https://doi.org/10.1016/j.surfcoat.2022.128402.
7) Kiliszkiewicz M, Domaradzki J, Posadowski W, Mazur M, Wiatrowski A, Dawidowski W, et al. Effect of sputtering power and oxygen partial pressure on structural and opto-electronic properties of Al-doped ZnO transparent conducting oxides. *Applied Surface Science*. 2024;670:160601. https://doi.org/10.1016/j.apsusc.2024.160601.
8) Lai FI, Yang JF, Hsu YC, Kuo SY. Location-optoelectronic property correlation in ZnO:Al thin film by RF magnetron sputtering and its photovoltaic application. *Materials (Basel)*. 2021;14(21):6313. https://doi.org/10.3390/ma14216313.
9) Mohammed AA, Khodair ZT, Khadom AA. Preparation and investigation of the structural properties of α-Al2O3 nanoparticles using the sol-gel method. *Chemical Data Collections*. 2020;29:100531. https://doi.org/10.1016/j.cdc.2020.100531.
10) Rahman MR, Uddin MN, Ashrafy T, Washif M, Uddin MR, Hoq M, et al. Tuning of optical band gap: genesis of thickness regulated Al doped ZnO nano-crystalline thin films formulated by sol-gel spin coating approach. *Transactions on Electrical and Electronic Materials*. 2022;23(3):205–218. https://doi.org/10.1007/s42341-021-00341-0.
11) Waikar MR, Shaikh AA, Sonkawade RG. The supercapacitive performance of woollen-like structure of CuO thin films prepared by the chemical method. *Vacuum*. 2019;161:168–175. https://doi.org/10.1016/j.vacuum.2018.11.057.
12) Al-Rasheidi M, Majid MA, Riaz S, Balobaid AS, Khan F. Development of MnxCo0.015Zn1-xO electron transport layer for perovskite solar cells: Experimental and simulation study. *Optical Materials*. 2023;143:114281. https://doi.org/10.1016/j.optmat.2023.114281.
13) Razva O, Anufrienkova A, Korovkin M, Ananieva L, Abramova R. Environmental problems of oil fields and application of geothermal water in agriculture. *IOP Conference Series: Earth and Environmental Science*. 2014;21:012006. https://doi.org/10.1088/1755-1315/21/1/012006.
14) Regmi G, Rijal S, Velumani S. Aluminum-doped zinc oxide (AZO) ultra-thin films deposited by radio frequency sputtering for flexible Cu(In,Ga)Se2 solar cells. *Memories*. 2023;5:100064. https://doi.org/10.1016/j.memori.2023.100064.
15) Poddar NP, Mukherjee SK. Ultraviolet-A-transparent aluminum-doped zinc oxide thin film electrodes by pulsed laser deposition: Effect of substrates and post-deposition annealing. *Journal of Materials Science: Materials in Electronics*. 2019;30:14269–14280. https://doi.org/10.1007/s10854-019-01796-x.
16) Rahman MM, Rahman KS, Rokonuzzaman M, Bhari BZ, Ludin NA, Ibrahim MA. Impact of aluminium doping in magnesium-doped zinc oxide thin films by sputtering for photovoltaic applications. *Journal of Materials Science*. 2024;59:9472–9490. https://doi.org/10.1007/s10853-024-09801-3.
17) Rana VS, Purohit LP, Sharma G, Singh SP, Sharma SK. Effect of RF Power on Physical and Electrical Properties of Al-doped ZnO Thin Films. *Indian Journal of Pure & Applied Physics*. 2022;60:246–253. https://doi.org/10.56042/ijpap.v60i3.57873.

18) Mazur M, Kiliszkiewicz M, Posadowski W, Domaradzki J, Małachowska A, Sokołowski P. A Comprehensive Investigation of the Mechanical and Tribological Properties of AZO Transparent Conducting Oxide Thin Films Deposited by Medium Frequency Magnetron Sputtering. *Materials*. 2024;17(1):81. https://doi.org/10.3390/ma17010081.
19) Parhana P. Effect of Substrate Temperature on Structural, Optical and Electrical Properties of AZO Thin Films by RF Magnetron Sputtering for Optoelectronic Devices. *International Journal of Research in Applied Science and Engineering Technology*. 2025;13:1371–1375. https://doi.org/10.22214/ijraset.2025.67562.
20) Potocnik J, Novakovic M, Popovic M. Thickness-dependent growth of Ni vertical columns deposited by GLAD method: Study on the microstructural and optical properties. *Optical Materials*. 2024;154:115665. https://doi.org/10.1016/j.optmat.2024.115665.
21) Kumar A, Gorai DK, Kumar B, Kundu TK, Ahmad MI. Impact of Al-Tl co-doping on the Optoelectronic Properties of ZnO thin film: Experimental and DFT Approach. *Materials Chemistry and Physics*. 2025;p. 130908. https://doi.org/10.1016/j.matchemphys.2025.130908.
22) Rekkache H, Mezrag S, Fellah M, Bouarissa N, Bouaballou A, Kaci S, et al. Characterization of RF magnetron sputtered pure and aluminum-doped zinc oxide thin films for optoelectronic applications. *Journal of Materials Science: Materials in Electronics*. 2025;36:934. https://doi.org/10.1007/s10854-025-15004-6.
23) Li X, Tang W, Chen C, Lin C, Xu C. Effect of annealing treatment on the structure and performance of transparent conductive AZO/Al2O3 bi-layer films. *Materials Research Express*. 2019;6(9):096414. https://doi.org/10.1088/2053-1591/ab2e58.
24) Badgujar AC, Yadav BS, Jha GK, Dhage SR. Room temperature sputtered aluminum-doped ZnO thin film transparent electrode for application in solar cells and for low-band-gap optoelectronic devices. *ACS Omega*. 2022;7(16):14203–14210. https://doi.org/10.1021/acsomega.2c00830.
25) Lokhande SD, Awale MB, Umadevi G, Mote VD. Effect of Ni doping on structural, optical and gas sensing properties of ZnO films for the development of acetone sensor devices. *Materials Chemistry and Physics*. 2023;301:127667. https://doi.org/10.1016/j.matchemphys.2023.127667.
26) Sener E, Bayram O, Hasar UC, Simsek O. Structural and optical properties of RF sputtered ZnO thin films: Annealing effect. *Physica B: Condensed Matter*. 2021;605:412421. https://doi.org/10.1016/j.physb.2020.412421.
27) Mozaffari N, Elahi SH, Parhizgar SS, Mozaffari N, Elahi SM. The effect of annealing and layer numbers on the optical and electrical properties of cobalt-doped TiO2 thin films. *Materials Research Express*. 2019;6(11):116428. https://doi.org/10.1088/2053-1591/ab4662.
28) Fasasi AY, Ajenifuja E, Osagie E, Animasaun LO, Adeoye AE, Obiajunwa EI. Optical, dielectric and optoelectronic properties of spray deposited Cu-doped Fe2O3 thin films. *Journal of the Nigerian Society of Physical Sciences*. 2023;5:1180. https://doi.org/10.46481/jnsps.2023.1180.
29) Yaseen M, Farooq Z, Ahmad M, et al. Synthesis and investigation of linear and nonlinear optical properties of an octahedral metalloporphyrin. *Optical Materials*. 2024;149:115092. https://doi.org/10.1016/j.optmat.2024.115092.
30) Bhari BZ, Chelvanathan P, Ludin NA, Ibrahim MA, Rahman KS. Elucidating the microstructural and optoelectronic properties evolution of sputtered Al-doped MZO thin films. *Physica B: Condensed Matter*. 2025;697:416703. https://doi.org/10.1016/j.physb.2024.416703.
31) Dejam L, Sabbaghzadeh J, Ghaderi A, et al. Advanced nano-texture, optical bandgap, and Urbach energy analysis of NiO/Si heterojunctions. *Scientific Reports*. 2023;13:6518. https://doi.org/10.1038/s41598-023-33713-y.
32) Khamee W, Niyom K, Rattanasakulthong W. Thickness dependence of optical properties of sputtered AZO film on borosilicate glass. *Journal of Physics: Conference Series*. 2023;2653:012046. https://doi.org/10.1088/1742-6596/2653/1/012046.
33) Khlayboonme ST, Thowladda W. Impact of Al-doping on structural, electrical, and optical properties of sol-gel dip coated ZnO:Al thin films. *Materials Research Express*. 2021;8:076402. https://doi.org/10.1088/2053-1591/ac113d.